Force Field for Mica-Type Silicates and Dynamics of Octadecylammonium Chains Grafted to Montmorillonite

Hendrik Heinz,*[,†,‡] Hilmar Koerner,[†,§] Kelly L. Anderson,[†] Richard A. Vaia,[†] and B. L. Farmer[†]

Materials and Manufacturing Directorate, Air Force Research Laboratory, Wright Patterson AFB, Dayton, Ohio 45433, Department of Mechanical and Materials Engineering, Wright State University, Dayton, Ohio 45435, and University of Dayton Research Institute, Dayton, Ohio 45469

Received May 3, 2005. Revised Manuscript Received August 2, 2005

Layered silicates are widely used in nanotechnology and composite materials. We describe a force field for phyllosilicates (mica, montmorillonite, and pyrophyllite) on the basis of physically justified atomic charges, van der Waals parameters, vibrational constants, and distributions of charge defects in agreement with solid state ^{29}Si NMR data. Unit cell parameters deviate only ~0.5% relative to experimental X-ray measurements and surface (respectively cleavage) energies deviate less than 10% from experimental data, including the partition between Coulomb and van der Waals contributions. Reproduction of surface energies facilitates quantitative simulations of hybrid interfaces with water, organics, and biomolecules for which accurate force fields are available. Parameters are consistent with the force fields PCFF (polymer consistent force field), CVFF (consistent valence force field), CHARMM (chemistry at Harvard macromolecular mechanics), and GROMACS (Groningen machine for chemical simulations). As an example of interest, we investigate the structure and dynamics of octadecylammonium montmorillonite ("C_{18}"−montmorillonite, cation exchange capacity = 91 mmol/100 g) by molecular dynamics simulation. The surfactant chains assemble essentially as a bilayer with minimal interpenetration within the gallery while the ammonium headgroups are hydrogen-bonded to cavities in the montmorillonite surface. In contrast to quaternary ammonium ions, no rearrangements on the surface have been observed (cavity crossing barrier >5 kcal/mol). The alkyl chains are in a liquidlike state with approximately 30% gauche conformations, in agreement with previous Fourier-transform infrared and solid-state NMR measurements. Computed X-ray diffraction patterns of sodium and C_{18}−montmorillonite agree very well with X-ray patterns from experiment, and the computational model can assist in the assignment of complex reflections.

1. Introduction

Layered silicates are used industrially in greases, paints, and drilling fluids, as well as in polymer−clay nanocomposites for plastics, rubbers, and thin films.[1,2] Applications range from cosmetics, packaging materials, and commodities to aerospace and automotive parts. A common nanoscale reinforcement for polymer-layered silicate composites are organically modified montmorillonites where alkali cations in the galleries are replaced by primary or quaternary alkylammonium cations.[3−6] Similar sheet silicates such as mica and pyrophyllite are frequently used as fillers for nanocomposites[2] and as model systems for interfaces with aqueous solutions, surfactants, polymers, or friction under confinement.[7−9] Recent attempts are directed toward controlling the orientation of aluminosilicate sheets in nanocomposites through application of magnetic fields[6] in the molten state.

Molecular simulations at the atomistic level are useful to complement experimental data on the structure and interface properties of nanostructured materials. On the basis of accurate force fields, simulations often provide (semi)-quantitative predictions, for example, coordination geometries and dynamical behavior at inorganic−organic interfaces, interface tensions and adsorption energies, orientational correlation functions, elastic constants, or parameters for coarse-grained and multiscale models.[10−27]

Although several classical atomistic models for (alumino)-silicates have been developed over the years,[13−23] a number

---

* Corresponding author. E-mail: hendrik.heinz@wright.edu.
[†] Wright Patterson AFB.
[‡] Wright State University.
[§] University of Dayton Research Institute.

(1) *Nanoscale Materials*; Liz-Marzan, L. M., Kamat, P. V., Eds.; Kluwer: Boston, 2003.
(2) Wypych, G. *Handbook of Fillers*, 2nd ed.; ChemTec Publishing: Toronto, ON, Canada, 1999.
(3) Vaia, R. A.; Ishii, H.; Giannelis, E. P. *Chem. Mater.* **1993**, *5*, 1694−1696.
(4) Vaia, R. A.; Teukolsky, R. K.; Giannelis, E. P. *Chem. Mater.* **1994**, *6*, 1017−1022.
(5) Fong, H.; Vaia, R. A.; Sanders, J. H.; Lincoln, D.; Vreugdenhil, A. J.; Liu, W. D.; Bultman, J.; Chen, C. G. *Chem. Mater.* **2001**, *13*, 4123−4129.
(6) Koerner, H.; Jacobs, D.; Tomlin, D. W.; Busbee, J. D.; Vaia, R. A. *Adv. Mater.* **2004**, *16*, 297−300.
(7) Osman, M. A.; Ernst, M.; Meier, B. H.; Suter, U. W. *J. Phys. Chem. B* **2002**, *106*, 653−662.
(8) Maeda, N.; Chen, N. H.; Tirrell, M.; Israelachvili, J. N. *Science* **2002**, *297*, 379−382.
(9) Raviv, U.; Klein, J. *Science* **2002**, *297*, 1540−1543.
(10) Berendsen, H. J. C.; van der Spoel, D.; van Drunen, R. *Comput. Phys. Commun.* **1995**, *91*, 43−56.
(11) MacKerell, A. D.; et al. *J. Phys. Chem. B* **1998**, *102*, 3586−3616.
(12) Mahoney, M. W.; Jorgensen, W. L. *J. Chem. Phys.* **2000**, *112*, 8910−8922.
(13) Sanders, M. J.; Leslie, M.; Catlow, C. R. A. *J. Chem. Soc., Chem. Commun.* **1984**, 1271−1273.
(14) Catlow, C. R. A.; Price, G. D. *Nature* **1990**, *347*, 243−248.
(15) Collins, D. R.; Catlow, C. R. A. *Am. Mineral.* **1992**, *77*, 1172−1181.
(16) Beest, B. W. H.; Kramer, G. J.; Van Santen, R. A. *Phys. Rev. Lett.* **1990**, *64*, 1955−1958.

10.1021/cm0509328 CCC: $30.25

Table 1. Parameters and Their Primary Effect in Force Fields for Minerals

parameter	effect on the simulation
atomic charges	surface energy, interface structure, adsorption energies, long-range effects
equilibrium nonbond energy (Lennard-Jones well depth)	surface energy, interface structure, adsorption energies
vibrational constants	elastic properties, lattice dynamics
distribution and parametrization of charge defects	interfacial properties and dynamics
compatibility of the energy expression with force fields for (bio)organic compounds	scope of application

of essential problems have not been addressed sufficiently (Table 1): (1) assumptions for atomic charges are in a wide range, for example, Si in tetrahedral oxygen coordination varies from +0.5 to +4.0; (2) van der Waals parameters are poorly validated, for example, well depths for Si range from 0.0 to 0.4 kcal/mol; (3) principal vibrational constants differ by several 10%; (4) the distribution and parametrization of charge defects in the minerals are handled in empirical ways; and (5) force field parameters are often not compatible with existing force fields for (bio)organic molecules and polymers.

As a consequence, calculated crystal geometries, surface energies, elastic constants, and dynamical properties commonly differ significantly from experimental observations. In particular, interfacial properties in nanostructured hybrid materials are of increasing interest. They can be computed correctly when the surface energy (or another form of cohesive energy) of each component is reproduced in a simulation, which is sensitive to the nonbond parameters, that is, atomic charges and van der Waals parameters. Unfortunately, these quantities often deviate up to 1 order of magnitude from experimental values in common force fields. Our aim is to introduce a thoroughly reliable, widely compatible force field for mica-type silicates, based on some earlier steps in this direction.[24−27]

Thereafter, we consider an example of practical interest, the structure and dynamics of montmorillonite modified with octadecylammonium ions (C_{18}−montmorillonite). This material is used in the fabrication of polymer nanocomposites, and we explain experimental data [IR, X-ray, NMR, differential scanning calorimetry (DSC)] on the basis of molecular dynamics (MD) simulation.

Table 2. Force Field Parameters for Mica, Montmorillonite, and Pyrophyllite, According to Equation 1 (PCFF)[a]

I. nonbond	charge[b] (*e*)	r_0 (pm)	E_0 (kcal/mol)
K	+1.0	410 [380]	0.20 [0.20]
Na	+1.0	330 [310]	0.06 [0.06]
$Si^{surface}$	+1.1	420 [400]	0.035 [0.05]
$Al^{surface}$	+0.8	450 [420]	0.035 [0.05]
$Al^{octahedral}$	+1.45		
$Mg^{octahedral}$	+1.1	450 [420]	0.035 [0.05]
$O^{surface}$	−0.55 (−0.783 33[c])	380 [350]	0.015 [0.025]
O^{apical}	−0.758 33 (−0.866 66[d])		
$O^{hydroxyl}$	−0.683 33 (−0.791 66[d])		
$H^{hydroxyl}$	+0.20	109.8 [109.8]	0.013 [0.013]

II. Bonds	r_0 (pm)	k_r [kcal/(mol·Å^2)]
all bonds between Si, O, Al, Mg[e]	exptl[e]·1.05	860
O−H	92.9	990

III. angles	θ_0 (deg)	k_θ [kcal/(mol·rad^2)]
all angles between Si, O, Al, Mg[e]	exptl[e]	340
H−O−Al	116.2	23

[a] For the force fields CVFF, CHARMM, and GROMACS with a 12-6 Lennard-Jones potential (eq 2), the van der Waals parameters in square brackets apply. [b] Reference 24. Excessive decimals are included to maintain overall charge neutrality. [c] When bonded to Al defect. [d] When bonded to Mg defect. [e] Reference 37. The experimental value refers to the bond lengths and angles as given in the X-ray crystal structure.

The outline of this paper is as follows. In section 2, we discuss the physical meaning and assignment of our force field parameters for the dioctahedral phyllosilicates mica, montmorillonite, and pyrophyllite, followed by extensive evaluation. In section 3, we apply the extended polymer consistent force field (PCFF) to study the structure and dynamics of C_{18}−montmorillonite, including hydrogen bonding to the surface, chain conformations, temperature dependence, and analysis of X-ray data. Computational and experimental details are given separately in each section. We conclude with a summary in section 4.

2. Force Field and Validation

In this section, a new force field for phyllosilicates is presented. We begin with an outline of the concepts and general aspects for the derivation of the force field, describe computational and experimental details, discuss the energy expression and the assignment of individual parameters in detail, and conclude with an evaluation of the performance.

2.1. Concept. Our approach to the major challenges listed in Table 1 is the following.

(1) The interpretation and assignment of atomic charges in classical simulations of polar systems was recently addressed by Heinz and Suter.[24] There is systematic evidence that atomic charges can be determined experimentally with an accuracy of roughly ±0.1*e* and such charges are most suited for corresponding force fields. In agreement with experiment and a novel theoretical concept (the extended Born model), atomic charges for our phyllosilicates were assigned with an accuracy of ±0.1*e* to ±0.2*e* (Table 2).[24]

---

(17) (a) Hill, J. R.; Sauer, J. *J. Phys. Chem.* **1994**, *98*, 1238−1244. (b) Hill, J. R.; Sauer, J. *J. Phys. Chem.* **1995**, *99*, 9536−9550.

(18) Teppen, B. J.; Rasmussen, K.; Bertsch, P. M.; Miller, D. M.; Schafer, L. *J. Phys. Chem. B* **1997**, *101*, 1579−1587.

(19) (a)Skipper, N. T.; Refson, K.; McConnell, J. D. C. *J. Chem. Phys.* **1991**, *94*, 7434−7445. (b)Greathouse, J. A.; Refson, K.; Sposito, G. *J. Am. Chem. Soc.* **2000**, *122*, 11459−11464. (c)Park, S. H., Sposito, G. *Phys. Rev. Lett.* **2002**, *89*, 085501.

(20) Kuppa, V.; Manias, E. *Chem. Mater.* **2002**, *14*, 2171−2175.

(21) (a) deLeeuw, N. H.; Manon Higgins, F.; Parker, S. C. *J. Phys. Chem. B* **1999**, *103*, 1270−1277. (b)Fang, C. M.; Parker, S. C.; De With, G. *J. Am. Ceram. Soc.* **2000**, *83*, 2082−2084. (c)Sayle, D. C.; Parker, S. C. *J. Am. Chem. Soc.* **2003**, *125*, 8581−8588.

(22) Cygan, R. T.; Liang, J. J.; Kalinichev, A. G. *J. Phys. Chem. B* **2004**, *108*, 1255−1266.

(23) Manevitch, O. L.; Rutledge, G. C. *J. Phys. Chem. B* **2004**, *108*, 1428−1435.

(24) Heinz, H.; Suter, U. W. *J. Phys. Chem. B* **2004**, *108*, 18341−18352.

(25) Heinz, H.; Castelijns, H. J.; Suter, U. W. *J. Am. Chem. Soc.* **2003**, *125*, 9500−9510.

(26) Heinz, H.; Paul, W.; Suter, U. W.; Binder, K. *J. Chem. Phys.* **2004**, *120*, 3847−3854.

(27) Heinz, H.; Suter, U. W. *Angew. Chem., Int. Ed.* **2004**, *43*, 2239−2243.

Preliminary evaluation demonstrated improvements in reproduction of geometry and phase behavior of organically modified micas in agreement with experimental data [X-ray diffraction (XRD), near-edge x-ray absorption fine structure, NMR, IR, DSC], and further evidence will be presented here.[8,25−27]

(2) To the best of our knowledge, we are first to consider surface and cleavage energies in the design of atomistic models for inorganic surfaces.[28] Surface tensions are primary thermodynamic characteristics of surfaces and determine interfacial processes in mixtures with other components.[29−33] For the quantitative simulation of such interfaces, surface and cleavage energies in mineral models must, therefore, be physically realistic. Besides, classical surface theory divides surface tensions into polar (electrostatic) and dispersive (Lifschitz−van der Waals) contributions,[30−33] for which appropriate energy terms in classical force fields are available (see eqs 1 and 2), allowing the analysis of such partitions. To achieve that goal, it is important to assign physically justified van der Waals parameters (dispersive contribution) next to reliable atomic charges (polar contribution). On the basis of available concepts, we discuss the physical meaning of van der Waals parameters and fine-tune the parameters to fit experimental data on surface tensions and cleavage energies.[32−34] The exceptional ability of layered silicates to form even, defect-free surfaces that extend over micrometers warrants reasonably accurate experimental results.[9,25,32,33]

(3) We refine vibrational constants by comparison of computed IR spectra from the velocity of the autocorrelation function to experimental IR spectra.

(4) The distribution of $[SiO_4] \rightarrow [AlO_4]^-\cdots K^+$ charge defects in the tetrahedral layer is parametrized according to available ^{29}Si NMR data.[27] $[AlO_6] \rightarrow [MgO_6]^-\cdots Na^+$ defects in the octahedral layer of the phyllosilicates are treated analogously.

(5) The primary force field under consideration is the PCFF,[35] which contains a 9-6 Lennard-Jones potential and is well-parametrized for alkyl chains, organic residues, and polymers.[25,35] The force fields consistent valence force field (CVFF),[35] CHARMM (chemistry of Harvard macromolecular mechanics),[11] and GROMACS (Groningen machine for chemical simulations),[10] which employ a 12-6 instead of a 9-6 Lennard-Jones potential, are equally considered to ensure compatibility of our phyllosilicate parameters with the excellent parameters for organic and biological molecules.[10−12] The transfer from a 9-6 to a 12-6 Lennard-Jones potential requires slightly different Lennard-Jones parameters while the other parameters remain the same.

Our primary energy expression is based on the PCFF.[35] For the mineral, not all PCFF energy terms are required[25] and we consider only the following contributions (eq 1): quadratic bond stretching, quadratic angle bending, Coulomb energy, and a 9-6 nonbond potential with geometric combinations rules.

$$E_{\mathrm{pot}} = \sum_{ij\mathrm{bonded}} \frac{1}{2} K_{r,ij}(r_{ij} - r_{0,ij})^2 + \sum_{ijk\mathrm{bonded}} \frac{1}{2} K_{\theta,ijk}(\theta_{ijk} - \theta_{0,ijk})^2 + \frac{1}{4\pi\epsilon_0\epsilon_r} \sum_{\substack{ij\mathrm{nonbonded}\\ (1,3\mathrm{excl})}} \frac{q_i q_j}{r_{ij}} + \sum_{\substack{ij\mathrm{nonbonded}\\ (1,3\mathrm{excl})}} E_{0,ij}\left[2\left(\frac{r_{0,ij}}{r_{ij}}\right)^9 - 3\left(\frac{r_{0,ij}}{r_{ij}}\right)^6\right] \quad (1)$$

When the force fields CVFF, CHARMM, and GROMACS are used, the last term is a 12-6 Lennard-Jones potential instead (eq 2):

$$E_{\mathrm{pot}} = \sum_{ij\mathrm{bonded}} \frac{1}{2} K_{r,ij}(r_{ij} - r_{0,ij})^2 + \sum_{ijk\mathrm{bonded}} \frac{1}{2} K_{\theta,ijk}\,(\theta_{ijk} - \theta_{0,ijk})^2 + \frac{1}{4\pi\epsilon_0\epsilon_r} \sum_{\substack{ij\mathrm{nonbonded}\\ (1,3\mathrm{excl})}} \frac{q_i q_j}{r_{ij}} + \sum_{\substack{ij\mathrm{nonbonded}\\ (1,3\mathrm{excl})}} E_{0,ij}\left[\left(\frac{r_{0,ij}}{r_{ij}}\right)^{12} - 2\left(\frac{r_{0,ij}}{r_{ij}}\right)^6\right] \quad (2)$$

As we will see at the end of this section, these simple and computationally efficient expressions are suited for a surprisingly good force field. Next, we describe computational and experimental procedures in the derivation and validation of parameters and then their individual assignment.

2.2. Computational and Experimental Details. We employed the Cerius^2 graphical interface with the Discover program.[35] Unit cells of the minerals mica, montmorillonite, and pyrophyllite have been constructed according to the literature.[36−40] For preliminary calculations, a simple small unit cell can be used, but for final evaluations and parameter adjustment, supercells have been employed (as given in Table 3).

IR spectral frequencies and cell parameters were calculated by MD simulation using the NPT ensemble, three-dimensional periodic boundary conditions, $T = 298$ K, velocity

---

(28) Parker et al., in ref 21b, calculated the surface energy for spineland and found roughly 50% deviation from the experimental value. Further development of the force field to reproduce experimentally measured surface properties was not considered.

(29) Hirschfelder, J. O.; Curtiss, C. F.; Bird, R. B. *Molecular Theory of Gases and Liquids*; Wiley: New York, 1954.

(30) Van Oss, C. J.; Chaudhury, M. K.; Good, R. J. *Chem. Rev.* **1988**, *88*, 927−941.

(31) Israelachvili, J. N. *Intermolecular and Surface Forces*, 2nd ed.; Academic Press: London, 1992.

(32) Adams, A. W.; Gast, A. P. *Physical Chemistry of Surfaces*, 6th ed.; Wiley: New York, 1997.

(33) Giese, R. F.; van Oss, C. J. *Colloid and Surface Properties of Clays and Related Minerals*; Marcel Dekker: New York, 2002.

(34) Chassin, P.; Jounay, C.; Quiquampoix, H. *Clay Miner.* **1986**, *21*, 899−907.

(35) Accelrys, Inc. *Cerius^2* and *Discover* (programs) and *Discover User Guide*, version 96.0/4.0.0; Molecular Simulations, Inc.: San Diego, CA, 1996.

(36) Güven, N. *Z. Kristallogr.* **1971**, *134*, 196−212.

(37) Rothbauer, R. *Neues Jahrb. Mineral., Monatsh.* **1971**, 143−154.

(38) (a) Brown, G. *The X-ray Identification and Crystal Structures of Clay Minerals*; Mineralogical Society: London, 1961. (b) *Reviews in Mineralogy*; Bailey, S. W., Ed.; Mineralogical Society of America: Chelsea, MI, 1988; Vol. 19. See also http://www.webmineral.com.

(39) (a) Tsipurski, S. I.; Drits, V. A. *Clay Mineral.* **1984**, *19*, 177−193. Mg positions not correct. (b) The exact crystal structure of montmorillonite depends on the nature of the cations (Na^+, K^+, Ca^{2+}), charge density (in ref 39a: $K_{0.58}$), and presence of crystal water. Mainly the parameters c (roughly 9.9−10.3 Å) and β (roughly 95−100°) are affected.

(40) Lee, J. H.; Guggenheim, S. *Am. Mineral.* **1981**, *66*, 350−357.

Table 3. Cell Parameters for Phyllosilicates, Calculated from NPT MD for the Given Supercells and Compared to Experimental Data

mineral		cell dimensions	*a* (nm)	*b* (nm)	*c* (nm)	α (deg)	*β* (deg)	*γ* (deg)	*V* (nm^3)	rms dev (pm/atom)
mica	expt[a]	5 × 3 × 1	2.596	2.705	2.005	90	95.74	90	14.00	<1
	sim		2.585	2.690	2.004	89.45	95.33	90.01	13.87	20
$K_{0.4}$−montmorillonite	expt[b]	5 × 3 × 2	2.6	2.7	∼2.0	90	95−100	90	14	
	sim		2.582	2.685	2.061	89.98	96.12	90.02	14.21	
$Na_{0.4}$−montmorillonite	expt[b]	5 × 3 × 2	2.6	2.7	∼2.0	90	95−100	90	14	
	sim		2.580	2.683	1.913	89.96	96.05	90.02	13.19	
pyrophyllite	expt[c]	5 × 3 × 2	2.580	2.690	1.869	91.18	100.46	89.64	12.76	<1
	sim		2.586	2.691	1.872	90.65	101.18	90.06	12.78	15

[a] Reference 37. [b] References 38 and 39. The exact composition of the samples is not known; thus, data are approximate. [c] Reference 40.

Table 4. Surface and Cleavage Energies[a] (mJ/m^2) of the Minerals in the Experiment and Simulation with Different Force Fields[b]

	pyrophyllite			montmorillonite	mica	principal charge (*e*)		principal well depth (kcal/mol)		
ref	γ^{tot}	γ^{el}	γ^{vdW}	ΔE_{cleav}	ΔE_{cleav}	Si^{tet}	Al^{oct}	Si	Al	O
exptl	39.7[c]	5.8[c]	33.9[c]	50−200[d]	375[e]	1.2[f]	1.45[f]			
this work	40	8	32	140	380	1.1	1.45	0.03	0.03	0.015
13, 15		[155]				4	3	0[g]	0[g]	49[g]
16		[>30]		[>300]	[>500]	2.4				0.47[h]
17	−515	2	−517	−3000	−433	0.52	1.33	0	0	0
18	−1094	13	−1107	−433	−162	1.4	1.68	0	0	6.86
19		[>15]				1.2	3	0[i]	0[i]	*i*
20		[>15]				1.2	2.8	*j*	*j*	*j*
22	81	30	51	167	484	2.1	1.58	10^{-6}	10^{-6}	0.155
23	265	155	110	251	683	4	3	0.04	9.04	0.228
25	260	8	252	340	631	1.1	1.45	0.40	0.50	0.06

[a] Pyrophyllite contains no alkali cations so that surfaces remain practically unchanged upon separation of the sheets, therefore the surface tension ($\gamma^{tot} = \gamma^{el} + \gamma^{vdW}$) is directly obtained as $^1/_2$ the energy difference upon infinite separation of two sheets. Montmorillonite and mica contain alkali cations between the sheets that change their positions upon sheet separation (surface reconstruction), therefore equivalent cleavage energies ΔE_{cleav} are obtained. [b] Estimates are given in square brackets. Force field parameters of major influence (charges and equilibrium nonbond energies) are specified. [c] Reference 33. [d] References 33 and 34. The exact value depends on the CEC. [e] Reference 32. [f] Reference 24. [g] Mixture of Buckingham potentials in ref 15. [h] Buckingham potential (three parameters). [i] Extended Buckingham potential (four parameters); O−O parameters not given. [j] Si−Si, Al−Al, and O−O van der Waals parameters not given.

scaling, a time step of 1 fs, Ewald summation for Coulomb interactions (accuracy 10^{-2} kcal/mol), and a cutoff for van der Waals interactions at 1.2 nm. For IR spectra, we collected snapshots every 3 fs for a total trajectory length of 5 ps, calculated the velocity autocorrelation function (VACF) involving all atoms, and performed the Fourier transform. To calculate cell parameters, snapshots were taken every 200 fs for a duration between 50 and 100 ps so that deviations in block averages were lower than 0.1%.

The calculation of surface energies for pyrophyllite was performed both through single point energy evaluations and MD (NVT ensemble), with high accuracy of the Ewald summation of Coulomb interactions (10^{-6} kcal/mol) and the same van der Waals cutoff at 1.2 nm. The difference between the (average) energies for two sheets adjoined and separated by 10 nm was calculated (three-dimensional periodic box with a long *c* axis of 100 nm). Differences between the single point and the MD approach are negligible (<1%), because pyrophyllite sheets undergo minimal changes during MD and no interlayer cations are present. The energy difference is independent from the separation path chosen and equals two times the surface tension (two identical surfaces moving apart).

The calculation of cleavage energies for montmorillonite and mica is more complex because interlayer cations change their positions. Sheet separation and equilibration was performed in very small steps. For any path chosen, however, the start and end points turn out to be the same, or convertible through some minimization steps when different force fields were employed for the comparison in Table 4. Thus, the start and end points were calculated essentially once and refined for use with different force fields. The energy difference corresponds to the cleavage energy; it differs from a surface energy through surface reconstruction. Cleavage energies are normalized to one surface in the same fashion as surface tensions. More details will be given in a separate publication.[51]

The Southern Clay montmorillonite IR spectrum has been experimentally measured as an average of 32 scans with overall resolution of 4 cm^{-1}, using a Nexus 470 Fourier transform infrared spectrometer. The sample was prepared from 2 mg of dried powderized montmorillonite [Southern Clay, cation exchange capacity (CEC) = 91 mmol/100 g] and 200 mg of KBr, pressed to an optically clear tablet.

2.3. Bonds and Angles. Equilibrium bond lengths r_0 and angles θ_0 can be obtained from experimental crystal structures with fractional atom coordinates for the unit cell or, with somewhat more uncertainty, from models optimized with ab initio methods.[41] We consider crystal structures for

---

(41) Aray, Y.; Marquez, M.; Rodriguez, J.; Coll, S.; Simon-Manso, Y.; Gonzalez, C.; Weitz, D. A. *J. Phys. Chem. B* **2003**, *107*, 8946−8952.

(42) In ref 25, vibrational constants were approximated coarsely. However, results are not affected because no elastic properties were investigated.

(43) Huheey, J. E.; Keiter, E. A.; Keiter, R. L. *Inorganic Chemistry: Principles of Structure and Reactivity*, 4th ed.; Harper Collins: New York, 1993.

(44) Batsanov, S. S. *Inorg. Mater.* **2001**, *37*, 871−885.

(45) Halgren, T. A. *J. Am. Chem. Soc.* **1992**, *114*, 7827−7843.

(46) Rappe, A. K.; Casewit, C. J.; Colwell, K. S.; Goddard, W. A.; Skiff, W. M. *J. Am. Chem. Soc.* **1992**, *114*, 10024−10035.

(47) Miller, K. J.; Savchick, J. A. *J. Am. Chem. Soc.* **1979**, *101*, 7206−7213.

(48) Nagle, J. K. *J. Am. Chem. Soc.* **1990**, *112*, 4741−4747.

(49) Bilz, H.; Benedek, G.; Bussmann-Holder, A. *Phys. Rev. B* **1987**, *35*, 4840−4849.

(50) *CRC Handbook of Chemistry and Physics*, 84th ed.; Lide, D. R., Ed.; CRC Press: Boca Raton, 2003.

(51) Heinz, H.; Vaia, R.; Farmer, B. Submitted.

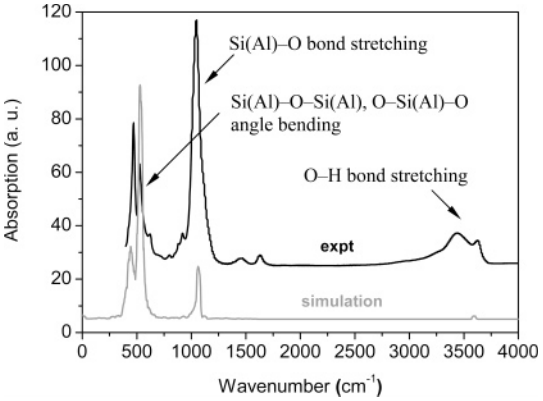

Figure 1. Experimental IR spectrum for Southern Clay montmorillonite (CEC = 91 mmol/100 g) and calculated IR spectrum for the atomistic model.

mica[36,37] $K_{1.0}[Si_3Al_1O_8][Al_2O_2(OH)_2]$, montmorillonite[38,39] $Na_{0.4}[Si_4O_8][Al_{1.6}Mg_{0.4}O_2(OH)_2]$, and pyrophyllite[40] $[Si_4O_8][Al_2O_2(OH)_2]$ to derive r_0 and θ_0 values. The framework of covalent bonds and angles is the same in all three minerals, and values for bond lengths and angles deviate by only a few percent from one mineral to another.[36−40] The small differences arise from varying amounts of charge defects and impurities, as well as uncertainty in the experimental measurements. Pyrophyllite contains no charge defects, montmorillonite contains predominantly $[AlO_6] \rightarrow [MgO_6]^-\cdots Na^+$ defects in the octahedral layer, and mica contains predominantly $[SiO_4] \rightarrow [AlO_4]^-\cdots K^+$ defects in the tetrahedral layer. The alkali ions compensate the one-electron deficiencies at each defect site and are located between the clay lamellae. A detailed description of the charge distribution can be found in ref 24. For the best compatibility with all three minerals and lowest deviations, we consider the equilibrium bond lengths r_0 and equilibrium bond angles θ_0 from the crystal structure of Rothbauer.[37] Defect atoms are treated equal to nondefect atoms with regard to bonds and angles; there are no indications they would significantly distort the crystal lattice.[36−40] As a result of the variety of bonds and, in particular, angles, 18 force field types are defined (K^+, Na^+, two Al, Mg-def, two Si, Al-def, nine O, H).

When the force field is considered as a whole, the presence of simultaneous nonbond interactions (especially strong electrostatic attraction) tends to contract bond lengths and the unit cell by a few precent. For optimum reproduction, a scaling factor of 1.05 for all equilibrium bond lengths r_0 is employed (Table 2). Equilibrium bond angles θ_0 remain the same as in the experimental crystal structure. As a side effect of bond scaling, the intensity of the bond stretching vibration is lowered (Figure 1).

2.4. Vibrational Constants. Vibrational constants k_r and k_θ can be derived from ab initio calculations or from the experimental density of vibrational states (IR/Raman spectrum). We fit the vibrational constants for bond stretching k_r and angle bending k_θ to experimental IR data (Figure 1). For a two-body stretching vibration, the conversion between wavenumbers $\tilde{\nu}$ and the force constant k_r is possible with the relationship for a harmonic oscillator

$$\omega^2 = k_r/\mu \tag{3}$$

where ω is the angular frequency $\omega = 2\pi\nu$ (corresponding to the frequency ν) and μ the reduced mass $\mu = m_1m_2/(m_1 + m_2)$ of the two atoms bonded together (with masses m_1 and m_2). The complete formula reads as

$$k_r = \frac{m_1 m_2}{m_1 + m_2}(2\pi c\tilde{\nu})^2 \tag{4}$$

This relationship, however, is not suited for a three-body bending vibration (k_θ).

Alternatively, the effect of given individual force constants, either bond stretching or angle bending, on absorption(s) in the IR spectrum can be monitored using the Fourier transform of the VACF for a short MD trajectory. The procedure is as follows: (1) turn off all other vibrational constants, electrostatic, and van der Waals interactions by setting them to zero in the force field (for analyzing an angle bending vibration, the associated bond stretching constants must remain at their original values); (2) record a short MD trajectory (typically 5 ps NPT at intervals of 3 fs); (3) calculate the velocity autocorrelation function; and (4) carry out the Fourier transform.[35] The signal(s) found in the resulting IR spectrum originate only from the selected vibration, and adjusting the constant allows one to fine-tune the IR spectrum. This procedure shows the response of the system to a particular force constant and is, thus, suited as a guide to physically reasonable values. However, it cannot (yet) be used to calculate force constants from an experimental IR/Raman spectrum because the experimental peaks are broad and it is difficult to map the inverse Fourier transform to individual bond stretching and angle bending constants.

The most important experimentally obervable IR features are bands at ~1050 cm^{-1} and at ~500 cm^{-1} (Figure 1). The IR band at 1050 ± 50 is caused by bond stretching vibrations. To assign a spring constant k_r in the model, both eq 3 and the VACF method yield the same value $k_r = 860 \pm 20$ kcal/(mol·Å^2) as an average for all Si−O and Al−O stretching vibrations in the mineral (Table 2). Combined with all other terms in the force field, this average reproduces the experimental frequency of the IR band correctly, though with lower intensity (Figure 1). The IR band at 3600 cm^{-1} is caused by O−H stretching vibrations, represented through a constant $k_r = 990$ kcal/(mol·Å^2).

The IR band measured at 500 ± 50 cm^{-1} (Figure 1) with two strong absorptions is caused by angle bending. As a result of the complex sheet structure, phyllosilicates have a variety of bond angles, such as O−Si−O, Si−O−Si, Si−O−Al, and so forth, in chemically different environments. The VACF method suggests individual angle bending constants k_θ in a range of 340−700 kcal/(mol·rad^2) to reproduce experimental absorptions around 500 cm^{-1}. In the context of the entire force field, vibrations couple with each other and include contributions from nonbond interactions. The outcome is less predictable, and couplings may lead to additional bands in the calculated IR spectrum. In such cases, the vibrational constants may not be fine-tuned correctly or some nonbond parameters (Lennard-Jones) may have physically unreasonable values. For example, the Al−O−H vibration significantly affects the vibrational spectrum, owed to the approximate treatment of the hydroxyl group. Hydroxyl H atoms are likely to be H-bonded to adjacent O atoms in the octahedral layer and less localized than we assume in a model restricted to localized bonds. After careful evaluation of several 10^2 parameters sets, we suggest an average angle bending constant $k_\theta = 340$ kcal/(mol·rad^2) for all angle bending vibrations involving Si, Al, Mg, and O, and a low constant $k_\theta = 23$ kcal/(mol·rad^2) for Al−O−H, reflecting the high H mobility (Table 2).

Both experimental and computed IR spectra for mica, montmorillonite, and pyrophyllite are very similar because of the same covalent bonding framework so that Na−montmorillonite is sufficiently representative. As a result of our parameter assignment, vibrational frequencies agree well with experiment while intensities remain a difficult part to reproduce (Figure 1). The broad O−H stretching band in the experiment (3000−3600 cm^{-1}) is also observed in organically modified montmorillonite. We conjecture it originates from moisture or H bonding (delocalization) in the octahedral layer. IR spectra according to other force fields cannot be easily included for comparison because often parameters are missing[15,19,20,22] or force fields refer to other silicates with dissimilar IR spectra (SiO_2, zeolithes).[13,16,17] In some force fields,[18,23,25,42] the major vibrations at 1050 cm^{-1} and at 500 cm^{-1} are shifted up to several 100 cm^{-1} and additional bands are found. Deviations on the order of ±100 cm^{-1} to experiment were reported in biomolecular force fields such as CHARMM.[11] Computed IR spectra, on the basis of the velocity autocorrelation function, are a valuable tool to monitor the "fingerprint" range up to 4000 cm^{-1} for bond stretching and angle bending vibrations in force fields, as well as a guide to improve parametrizations.

2.5. Atomic Charges. We rely on previous assignments of partial charges in agreement with both experimental results and theory (Table 2).[24] Atomization energies and ionization energies of the constituting elements, as well as their coordination geometry in the mineral, provide the physical basis.[24] Fluctuations of bond and angle constants have a negligible effect on the charges ($<0.1\ e$).

2.6. van der Waals Parameters. The van der Waals energy is described by the last term in eqs 1 and 2. The nonbonded "radius" of the atoms r_0 is related to atom size and determines the repulsive part of the van der Waals energy;[43,44] the equilibrium nonbonded energy or well depth E_0 is related to the polarizability of the atoms and determines the dispersive part of the van der Waals nonbonded energy.[45] The determination of these constants is often quite empirical, especially for dispersive energies E_0.[44−48] Good estimates for r_0 can be obtained on the basis of a recent work by Batsanov,[44] and rough estimates for E_0 can be made on the basis of the work by Halgren,[45] as outlined below. Final parameters are fitted to reproduce the experimentally determined density and surface/cleavage energies of the minerals.

Batsanov[44] presented an extensive treatment of van der Waals radii r_0, including a compilation of average "equilibrium" and average "crystallographic" van der Waals radii across the periodic table, on the basis of experimental data and theoretical considerations. With a 9-6 Lennard-Jones potential (PCFF, eq 1), the "equilibrium" van der Waals radii are best suited to parametrize r_0 for polar solids. Electrostatic attractions in the energy expression as a whole reduce this "equilibrium" separation by 10−15%, leading approximately to the correct "crystallographic" van der Waals radii. Given an element and its electronic configuration (for example, K^+ at a charge of +1.0 is similar to Ar), Batsanov's table[44] provides useful values for r_0. To fine-tune the density and correct geometry of the sheet silicates, minor adjustments on the order of 10% are necessary (Tables 2 and 3). With a 12-6 Lennard-Jones potential (CVFF, CHARMM, GROMACS), r_0 values are slightly lower than with a 9-6 potential because the repulsive term is stronger (Table 2).

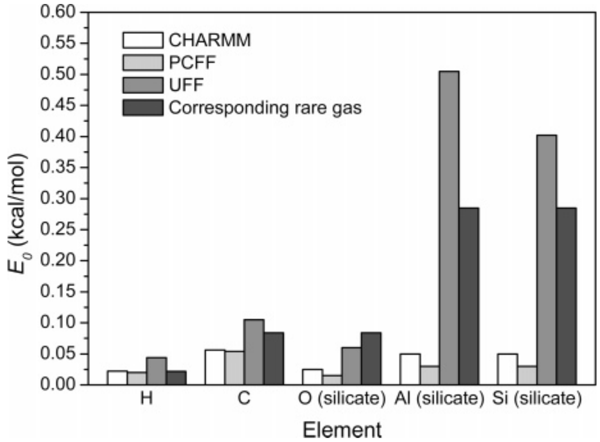

Figure 2. Well depths for selected elements (H···H, C···C, etc.) according to CHARMM, PCFF, and UFF, with reference values for the corresponding rare gases (He···He, Ne···Ne, Ar···Ar).

Attempts to estimate equilibrium nonbond energies E_0[29] have been made by Miller and Savchick,[47] Nagle,[48] Rappe et al.,[46] and Halgren;[45] however, it remains difficult to treat well depths E_0 systematically for all elements because they also depend on coordination geometry and atomic charges for the same element.[11,49,50] As a useful semiempirical rule, Halgren[45] suggests that the well depth E_0 for neutral elements rises uniformly toward E_0 of the respective rare gas within a row of the periodic table. Although exceptions can be found (e.g., transition metals with strong cohesion), this rule relates well depths for any element to accurately known E_0 values of rare gases for each row of the periodic table. We find the following procedure helpful to obtain a first guess for E_0: (1) Compare the electron configuration and polarizability of the element to the corresponding rare gas, considering Halgren's rule. (2) Consider the number of chemical bonds and atomic charges: high covalent coordination numbers strongly reduce E_0 because of many nearest neighbors (as compared to a rare gas), and positive charges reduce E_0 as a result of loss of available electron density for dispersion.

On the basis of these criteria, initial estimates of E_0 relative to the closest rare gases can be made. The final equilibrium nonbond energies (Table 2), however, are fine-tuned to reproduce the experimentally measured surface tension of pyrophyllite (contains no charge defects and no interlayer cations), as well as the cleavage energies for montmorillonite and mica (Table 4).[32−34,51] Comparison of these E_0 values (Si, Al, and O) to corresponding rare gas values indicates agreement within qualitative expectations (Figure 2). Well depths are distinctly lower than for corresponding rare gases, as a result of the dense covalent bonding framework and significant ionization. Equilibrium dispersive energies E_0 for the 12-6 nonbond potential (CHARMM, CVFF) are higher than for the 9-6 nonbond potential (PCFF), compensating for shorter 12-6 nonbond radii and stronger repulsion (Table 2). Benchmark values for C and H in saturated hydrocarbons, which are largely in agreement between PCFF,[35] CHARMM,[11] and GROMACS,[10,52] are also shown in Figure 2. Besides, we note that universal force field (UFF) parameters[46] are least suited (Figure 2).

Table 4 compares experimentally determined surface and cleavage energies for phyllosilicates to computed surface and cleavage energies with our force field and silicate force fields in the literature.[13,15−20,22,23,25] The evaluation of other force fields is in some cases difficult[13,15,16,19,20] because refs 13 and 16 refer to the simpler SiO_2 structure and some parameters are missing in refs 19 and 20. Reference 15 is an outgrow of ref 13 for mica, on the basis of a mixture of different Buckingham potentials, and ref 16 relies on a specialized Buckingham potential with four rather than two van der Waals parameters, which cannot be implemented in our program.[35] In these cases, estimates based on the accessible part of the parameters are given. In all other cases,[17,18,22,23,25] parameters were implemented in PCFF or CVFF and tested. The impact of atomic charges on surface energies is demonstrated by the polar contribution γ^{el} to the surface tension of pyrophyllite. If atomic charges are excessively small[17] or excessively large,[13,15,16,18−23] deviations of several multiples up to 1 order of magnitude are found, particularly when formal charges are employed.[13,15,23] The best value is obtained with our force field (Table 4). The impact of van der Waals parameters can be seen from the dispersive contribution γ^{vdW} to the surface tension of pyrophyllite. If Lennard-Jones parameters are excessively repulsive,[17,18] mineral sheets move apart from each other, corresponding to negative cleavage energies. If Lennard-Jones parameters are excessively attractive[23,25] (as recommended in UFF),[46] the van der Waals contribution to the surface energy γ^{vdW} is several times overestimated. The best value is obtained with our force field. Polar contributions, van der Waals contributions, and the net surface or cleavage energies are in good agreement with experimental observations. We have shown that nonbond parameters must be carefully evaluated, which is required to facilitate (semi)quantitative modeling of surface and interface processes.

2.7. Distribution of Charge Defects. The density and distribution of tetrahedral $[SiO_4] \rightarrow [AlO_6]^- \cdots K^+$ charge defects in mica and octahedral $[AlO_6] \rightarrow [MgO_6]^- \cdots Na^+$ charge defects in montmorillonite determine the properties of these minerals on the nanometer scale. Typically, every 4th tetrahedral silicon atom in mica (CEC = 251) and every 6th to every 4th octahedral aluminum atom in montmorillonite (CEC = 90−135) are substituted.[33] The distribution of such defects has been studied in detail in the tetrahedral layer of mica (Si → Al defects) using ^{29}Si NMR by Lipsicas et al., Sanz and Serratosa, and Herrero and Sanz[53−55] and was summarized elsewhere.[27] NMR spectral shifts indicate relative abundance of local environments of the Si atoms in the tetrahedral layer of mica (0 Al neighbors, one Al neighbor, and so forth). We assume transferability of the results to montmorillonite, where Al atoms in the octahedral layer are analogously surrounded by three metal neighbors through oxygen bridges. The defect distribution in a montmorillonite model with an average CEC = 108, $Na_{0.4}[Si_4O_8][Al_{1.6}Mg_{0.4}O_2(OH)_2]$, is shown in Figure 3. A total of 35% of the Al atoms are surrounded by three Al atoms and no Mg; 55% of the Al atoms are surrounded by two Al atoms and one Mg atom; 10% of the Al atoms are surrounded by one Al atom and two Mg atoms; and none of the Al atoms are surrounded by three Mg neighbors. Several defect distributions according to these data are possible, depending on the size of the model cell. All of them contain domains with a density of three defects per squared nanometer to a density of only one defect per squared nanometer (Figure 3).

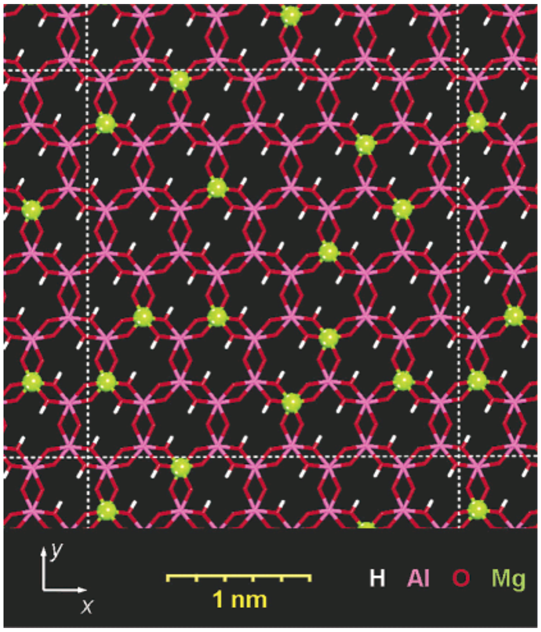

Figure 3. Octahedral layer of montmorillonite, viewed normal to the surface. An average distribution of Mg defects (highlighted) is shown.

2.8. Validation and Transferability. As a result of our parameter assignment, the force field (Table 2) reproduces experimental bond lengths and angles within a few percent deviation, and reproduction of vibrational frequencies is good in comparison to experiment (Figure 1). Unit cell parameters deviate on average ∼0.5%, while deviations between 1 and 5% are seen with other force fields (Table 3).[13−23,25] Surface or cleavage energies as well as its Coulomb and van der Waals contributions computed from the force field are in very good agreement with experimental data (Table 4). The successful implementation of these quantities for surface and interface thermodynamics corroborates the concepts to assign atomic charges[24] and to assign van der Waals parameters

---

(52) Different functional forms of the Lennard-Jones potential, such as 12-6 (CHARMM, GROMACS) or 9-6 (PCFF), do not significantly affect well depths if systems are of low polarity. A plot of these functions with the same parameters r_0 and E_0 illustrates this argument.

(53) Lipsicas, M.; Raythatha, R. H.; Pinnavaia, T. J.; Johnson, I. D.; Giese, R. F.; Constanzo, P. M.; Robert, J. L. *Nature* **1984**, *309*, 604−607.

(54) Sanz, J.; Serratosa, J. M. *J. Am. Chem. Soc.* **1984**, *106*, 4790−4793.

(55) Herrero, C. P.; Sanz, J. *J. Phys. Chem. Solids* **1991**, *52*, 1129−1135.

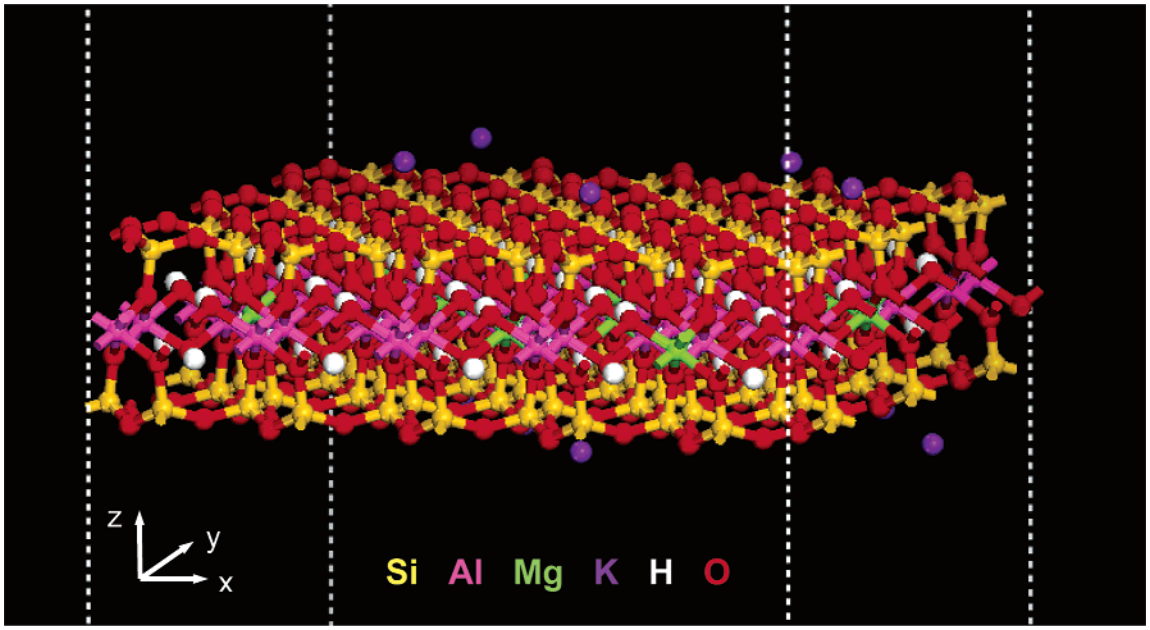

Figure 4. Structure and repeat (in the *xy* plane) of a single montmorillonite sheet used for the simulation. The dimensions of a single sheet are 2.60 nm × 2.70 nm × ~1 nm.

(section 2.6). The elimination of uncertainties on the order of multiples in surface energies and its components in force fields for minerals allows quantitative simulations of interfacial processes.

The distribution of charge defects is considered in detail (see ref 27 and Figure 3), and the parameters are embedded in force fields for organic and biological molecules: PCFF, CVFF, CHARMM, and GROMACS (Table 2). This facilitates the simulation of complex interfaces with water, organic molecules, polymers, amino acids, proteins, sugars, DNA, and other biologically important molecules. Differences between our parameters implemented in PCFF (9-6 Lennard-Jones potential) and implemented in CVFF, CHARMM, and GROMACS (12-6 Lennard-Jones potential) are negligible: simulated IR spectra are virtually the same (Figure 1), simulated cell parameters (Table 3) agree to experiment within 0.5%, and computed surface energies/cleavage energies (Table 4) agree to experiment within 5%.

3. Structure and Dynamics of C_{18}−Montmorillonite

Montmorillonite modified with octadecylammonium ions, n-$C_{18}H_{37}-NH_3^+$ (in the following called C_{18}), is one of the main components for clay−polymer nanocomposites. Understanding the structure and dynamics of the inorganic−organic interface is important with regard to possible modification and interactions with a polymer matrix.[3−9] We investigate the structure and dynamics of these inorganic−organic interfaces, as an application of the model outlined above. The composition of the model for montmorillonite is adjusted to match that of montmorillonite from Southern Clay Products with a CEC of 91 ± 10 mmol/100 g and the formula $Na_{0.33}[Si_{3.9}Al_{0.1}O_8][Al_{1.48}Fe_{0.225}Mg_{0.22}Ca_{0.01}\square_{0.065}O_2(OH)_2]$ ($\square$ = unknown from analysis). Our model formula is $Na_{0.333}[Si_4O_8][Al_{1.667}Mg_{0.333}O_2(OH)_2]$ with a CEC of 90 mmol/100 g. We neglect Fe in the octahedral layer and charge defects in the tetrahedral layer.

3.1. Computational and Experimental Details. A supercell with the above composition, the corresponding distribution of Mg defects,[27] and cell parameters listed in Table 2 (2.6 nm × 2.7 nm) was constructed. We cut out one of the two lamellae along with the appropriate number of alkali ions and rotated the structure around the *b* axis so that a cubic cell was obtained. The extension in the *c* direction amounts to 20 nm, much larger than the extension of the system, leaving the system effectively periodic in the *x* and *y* directions (Figure 4). This procedure allows the use of the NVT ensemble. It was verified earlier that the small difference in the pressure component p_{zz} relative to an NPT ensemble is negligible in the simulation (0 GPa vs 10^{-4} GPa), and uncertainties in selecting the barostat are eliminated.[26] To obtain equilibrium positions of the alkali counterions on the residual single sheet, we placed half of them 1 nm away on side and half of them 1 nm away on the other side of the lamella in several different arrangements and carried out molecular mechanics until convergence (lamella fixed). The structure with lowest energy was used in further simulations, assuming that the alkali ions had achieved their equilibrium positions.

Models of the ammonium ions n-$C_{18}H_{37}-NH_3^+$ were constructed with the Cerius^2 graphical interface, using default force field types.[35] The charges on the ammonium headgroup were derived as previously outlined in ref 24, leading to −0.5 for N, +0.4 for H, and +0.3 for C bonded to N.[56] The alkali ions on the montmorillonite surface were then replaced with the alkylammonium ions, whereby the ammonium headgroups occupy roughly the former positions of the alkali ions. Structures with different orientations of the alkyl tails relative to the surface were prepared. The structures are effectively periodic in the *x* and *y* directions while the *z* coordinate of the cubic box was set to 20 nm to avoid interactions in this

---

(56) Dipole moments for CH_3NH_2 and NH_3 indicate nitrogen charges of −0.70 and −0.80, respectively (ref 50).

direction (system height < 4 nm). After a short minimization to soften close contacts (100 steps, conjugate gradient method), MD simulations were performed: NVT ensemble, time step 1 fs, integration by Verlet algorithm, temperature control through velocity scaling, temperatures 298 and 373 K, van der Waals and Coulomb energy summation with the cell multipole method (octupoles, two layers of cells), and total duration 2−3 ns.[35] Thereafter, duplicate structures were generated and equilibrated again for 2−3 ns. Different starting structures converged to similar geometries and energies (<2 kcal/mol deviation per chain). The trajectories were recorded every 1 ps (1000 time steps). Coordinates of the last 500 snapshots were used to calculate density profiles, basal plane spacings, and average conformations (10 000 C_{18} ions and 160 000 torsions total).

For comparative conformational studies, models of octadecylamine were prepared in both the crystalline and the liquid state. A single molecule of octadecylamine was constructed with the Cerius^2 graphical interface, using PCFF default force field types. The charges at the headgroup were set to −0.8 for N, 0.3 for H, and 0.2 for C adjacent to the amino group.[55] A model of a unit cell for crystalline octadecylamine at 25 °C is difficult to build because no unit cell parameters could be found in the literature. We assume two outstretched n-$C_{18}H_{37}NH_2$ molecules in a tentative unit cell with the experimental density of 862 kg/m^3[3,50] oriented such that interaction between the ammonium headgroups is facilitated. This is similar to the structure of *n*-alkanes[57] and dimethyldioctadecylammonium bromide.[58,59] A 3 × 3 × 1 supercell (18 molecules) at 25 °C was subjected to NVT dynamics. The gauche/trans ratio of the chain backbones was analyzed, which is essentially the same for different unit cell geometries (alkyl chains are always parallel to each other). A model of the liquid octadecylamine at 100 °C was obtained by placing 30 molecules in a cubic box at a density of 850 kg/m^3[3,46] using the amorphous builder in Cerius,[31] followed by 1 ns of equilibration time (NVT dynamics) and 1 ns production time to analyze chain conformations.

XRD for determination of montmorillonite gallery spacings was conducted on a Bruker AXS D8 Discover at the Cu Kα wavelength of 1.5418 Å. The wide angle regime was collected using an evacuated Statton camera with a point-collimated X-ray beam via two pinholes (0.05 mm) at the Cu Kα wavelength of 1.5418 Å.

3.2. Results and Discussion. In the following, we discuss results from simulation and experiments. We begin with a qualitative description of the structure and dynamics and then follow up with quantitative indicators. Representative snapshots of the octadecylammonium−montmorillonite system are shown in Figures 5 (side view) and 6 (top view). The simulated structures have no periodicity in the *z* direction; thus, they include interfaces with a vacuum or an inert gas (10^{-3} times the density of the solid) on the top and on the bottom. The basal-plane spacing is freely equilibrated.

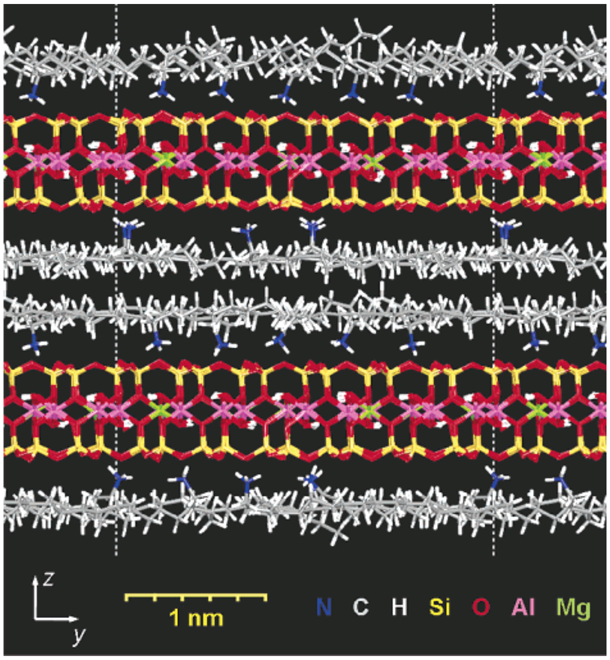

Figure 5. Snapshot (after 2 ns of simulation time) of the system C_{18}−montmorillonite−C_{18}−C_{18}−montmorillonite−C_{18} at 25 °C, viewed along the *x* direction. The formation of hydrocarbon monolayers on the clay surfaces can be seen, as well as hydrogen bonding of the ammonium headgroups to superficial oxygen atoms.

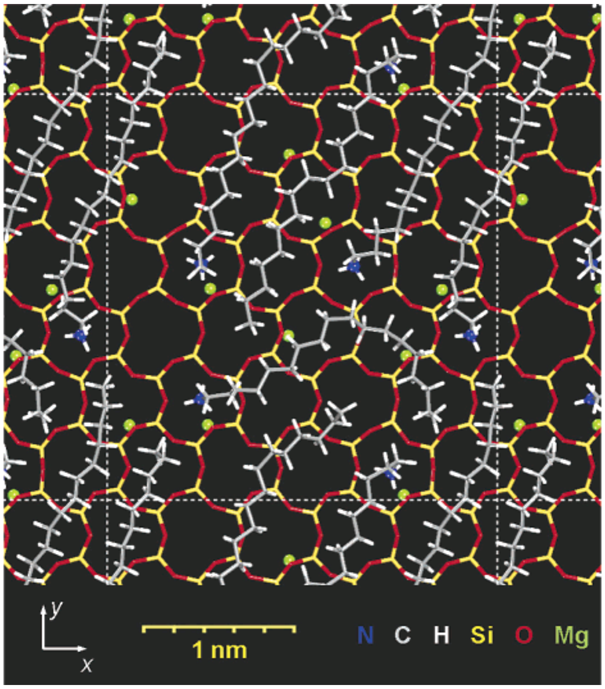

Figure 6. Top view (after 2 ns of simulation time) of the modified montmorillonite surface at 25 °C, viewed along the *z* direction. All the Mg charge defects in the octahedral layer (green pellets) but only the C_{18} chains on the top surface are shown.

Inorganic-organic interface. For most of the MD trajectory, alkylammonium ions lie flat on the mineral surfaces, forming essentially monolayers. Compared to mica where C_{18} chains stand upright as homogeneous tilted layers or islands,[25−27] the density of charge defects (and C_{18} chains) per surface area amounts to only 1/3 in montmorillonite (CEC = 91 for this montmorillonite vs CEC = 251 for mica), leading to this picture. As can be seen from Figure 6, the

---

(57) Boese, R.; Weiss, H. C.; Blaser, D. *Angew. Chem., Int. Ed.* **1999**, *38*, 988−992.

(58) Okuyama, K.; Soboi, Y.; Iijima, N.; Hirabayashi, K.; Kunitake, T.; Kajiyama, T. *Bull. Chem. Soc. Jpn.* **1988**, *61*, 1485−1490.

available surface area is not covered entirely, as a consequence of the CEC of this clay and the chain length (Figure 6). The position of the ammonium headgroups on the surface correlates with the position of the Mg charge defects in the octahedral layer (Figure 6). Headgroups prefer to be closely located above charge defects and avoid surface regions further away from defects. The likely reason is that Mg defects are less positively charged than Al (1.1 compared to 1.45) and the excess negative defect charge (1 e^-) is mainly distributed across the six oxygen atoms coordinated to Mg (Table 2).[24] This concentration of negative charge likely attracts the positively charged ammonium ions to the defect sites.

An interesting and so far unreported feature is the formation of hydrogen bonds between the ammonium headgroups and surface cavities in montmorillonite (Figures 5 and 6). RNH_3^+ groups are attached to the mineral surface by compensating the equivalent amount of $[AlO_6] \rightarrow [MgO_6]^-$ charge defects in the octahedral layer and additionally through hydrogen bonds between the $R-NH_3^+$ hydrogen atoms and oxygen atoms on the mineral surface. The three N-terminal hydrogen atoms are oriented toward the three nearest oxygen atoms of the superficial (Si, O) 12 rings, resulting in a relatively rigid coordination geometry (Figure 6). The average distance between surface oxygen atoms and ammonium hydrogen atoms amounts to 160−180 pm. In contrast to systems with peralkylated ammonium head groups,[25−27] the primary ammonium headgroups sit closer to the surface than the hydrocarbon tails. No rearrangements across cavities on the surface are observed in the course of the simulation (up to 5 ns). This indicates strong binding to the mineral surface, in agreement with dielectric spectroscopy measurements.[60] The absence of rearrangements in the simulation leads to an estimated barrier higher than 5 kcal/mol for crossover to another cavity.

XRD. Montmorillonite in its natural form (with Na^+ ions) and modified with octadecylammonium ions (C_{18}) has been characterized by XRD (Figure 7). The X-ray patterns are also computed from the atomistic models on the basis of atomic scattering factors (averaged over 20 configurations). For Na−montmorillonite, the experimental (001) peak is shifted to smaller angles than in the simulated pattern because H_2O is intercalated between montmorillonite sheets (which are hygroscopic), leading to increased basal plane spacing. All other experimental peaks match closely with those from simulation,[61] allowing interpretation aided by modeling results.

C_{18}−montmorillonite and Na−montmorillonite have a number of peaks in common, which arise from lattice spacings within single silicate sheets (Figure 7). Assignment of the reflections is confirmed through stepwise modifications of the model structure, such as considering only selected atoms (Si, Al, O), translating single sheets horizontally and vertically, and analyzing the response in the calculated X-ray pattern. Main contributions result from Si and Al lattice spacings; oxygen, nitrogen, and particularly hydrocarbons make no significant contribution because of their low scattering factors.[50,62] The marked peaks (003) in Figure 7 change upon organic modification: they shift to lower 2θ values with increasing intercalation of organic material, consistent with an increase in gallery height. Additionally, a broadening of the (003) reflection is observed (Figure 7). None of the XRD peaks other than (00*l*) can be attributed to reflections involving different sheets for the reason of turbostratic disorder.[63] Simulation, however, indicates an increased lateral mobility of the modified silicate sheets. Oscillations of ±70 pm in both the *x* and the *y* directions between two C_{18}−montmorillonite sheets are found while two Na−montmorillonite sheets oscillate less than ±10 pm in the horizontal direction.

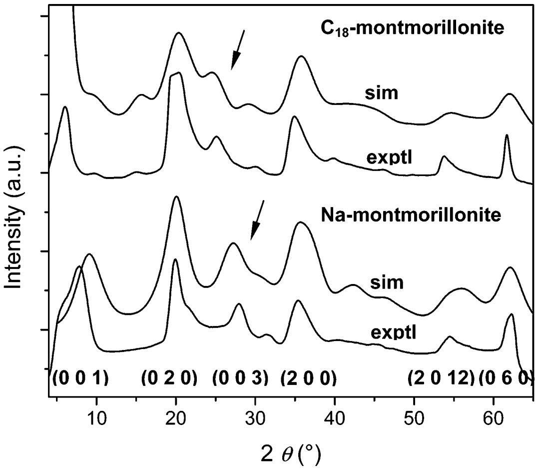

Figure 7. XRD patterns for Na−montmorillonite and C_{18}−montmorillonite in experiment (Southern Clay Products, CEC = 91) and simulation. The highlighted (003) lattice spacing is characteristic for the amount of intercalated material.

Conformational Analysis. The density profile of the C_{18}−montmorillonite system in the *z* direction is shown in Figure 8. The sharp peaks arise from montmorillonite, showing symmetrically two doublets from oxygen and silicon of the tetrahedral layer around a middle triplet by aluminum and oxygen in the octahedral layer of the lamellae. Each of the organic layers is characterized by a small peak due to the ammonium headgroups and a larger, relatively broad peak for the C_{18} hydrocarbon tail. The primary ammonium nitrogen is only 220 pm away from the superficial Si plane, compared to 380 pm for $(CH_3)_3N^+-C_{18}H_{37}$).[25,26] The distance from the basal plane (defined through octahedral Al) is 490 pm. Each hydrocarbon layer is approximately 400 pm thick. The two outer layers have somewhat more flexibility than the inner ones and appear slightly broadened (Figure 8). On heating to 100 °C, only minor differences are observed. The basal plane spacing increases slightly (Table 5), and the

---

(59) (a) Quantum mechanical methods are currently not able to predict crystal structures of organic molecules. Particularly in density functional theory, treatment of dispersive interactions is not yet sufficiently matured. See, for example: Zimmerli, U.; Parrinello, M.; Koumoutsakos, P. *J. Chem. Phys.* **2004**, *120*, 2693−2699. Trials with CASTEP or Dmol (ref 35) do not yield coherent results. (b) Cell parameters for crystalline *n*-octadecylamine could also not be unambiguously assigned in an extensive series of classical NPT MD simulations. The best values are $a = 0.47$ nm, $b = 0.44$ nm, $c = 5.4$ nm, $\alpha \approx 74°$, $\beta \approx 90°$, and $\gamma \approx 77°$.

(60) Jacobs, J. D.; Vaia, R. A.; Koerner, H.; Garrett, P. H. Submitted.

(61) The reflex module in $Cerius^2$ was used (ref 35).

(62) Pinnavaia, T.; Beall, G. W. *Polymer-Clay Nanocomposites*; John Wiley: New York, 2000.

(63) Moore, D. M.; Reynolds, R. C., Jr. *X-Ray Diffraction and the Identification and Analysis of Clay Minerals*; 2nd ed.; Oxford University Press: Oxford, 1997.

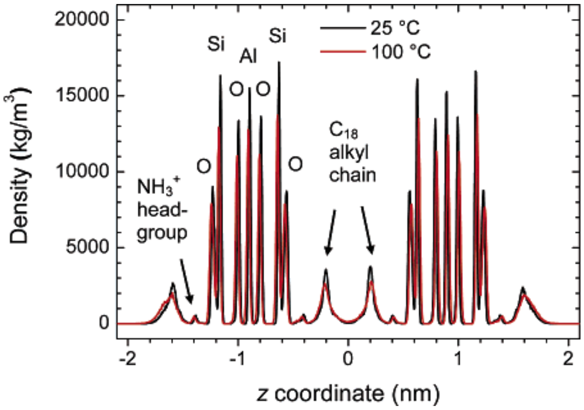

Figure 8. Density profile of the C_{18}−montmorillonite system at 25 and 100 °C.

Table 5. Basal Plane Spacings and Backbone Conformations

	basal plane spacing (nm)		gauche/C_{18}	
	25 °C	100°C	25 °C	100 °C
C_{18}−montmorillonite (exptl)	1.760 (10)	1.795 (10)		
C_{18}−montmorillonite (sim)	1.787 (5)	1.813 (8)	4.55 (1)	5.36 (1)
bulk octadecylamine			0.7 (1)	6.30 (1)

increased conformational freedom leads to broadening of the peaks in the density profile (Figure 8). Some alkyl chains cross into the adjacent hydrocarbon layer and extend the rest of their chain on the surface of the other sheet, effectively serving as a bridge between clay sheets. This effect is more pronounced at the higher temperature (100 °C) and persists to some extent on cooling.

Figure 9 shows the average distribution of torsional angles at 25 and at 100 °C, measured from the N atom of the ammonium headgroup toward the last carbon atom of the C_{18} chain (total 16 torsions per chain). At both temperatures, the average number of gauche bonds per chain backbone is remarkably high, between 4.5 and 5.4 per C_{18} backbone (Table 5). This indicates that the alkyl chains, which do not fill the total surface area for geometric reasons (Figure 6), are in a liquidlike state. For comparison, we also investigated the primary amine n-$C_{18}H_{37}NH_2$ in the bulk crystalline state at room temperature and as a melt at 100 °C (melting point 52.9 °C).[50] We find only 0.7 gauche incidences along the C_{18} backbone in the crystal and 6.3 in the liquid phase. Crystalline octadecylamine, thus, is very different from C_{18}−montmorillonite at 25 °C, and freely movable, liquid octadecylamine molecules at 100 °C, thus, exhibit somewhat more gauche torsions than C_{18} backbones tethered to montmorillonite, in agreement with expectation. Besides, in Figure 9, partition of the gauche torsional angles for liquid octadecylamine into two maxima is noticeable. This effect might be associated with the very high gauche fraction (40%) in the backbone, but it is not certain if the force field (which is in principle quite accurate for reproducing torsional angles)[25] gives the correct result. The existence of a liquidlike phase of C_{18} on montmorillonite at both temperatures is supported by solid-state ^{13}C NMR measurements (dominance of the ^{13}C chemical shift at 30 ppm)[64] and by the absence of a significant phase transition upon heating in DSC.[60] The alkyl chains are, under the given condition of confinement, in a significantly disordered state that does not allow for a phase transition to higher disorder under ambient conditions and 100 °C.

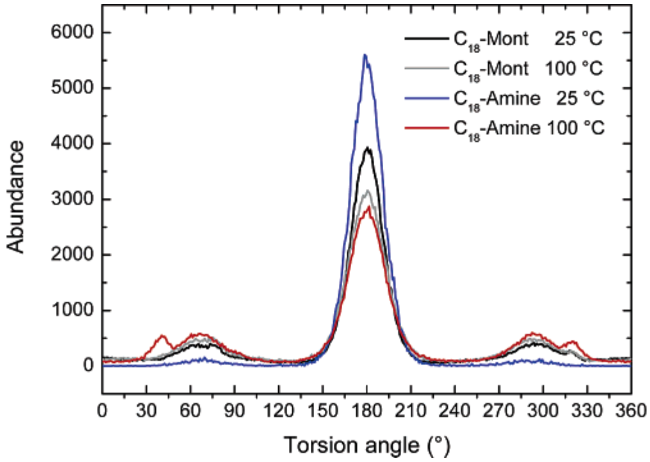

Figure 9. Distribution of torsional angles of the n-$C_{18}H_{37}$−NH_3^+ chains on montmorillonite. As a reference, the curves for solid and liquid octadecylamine (n-$C_{18}H_{37}$−NH_2) are also shown.

4. Conclusions

We presented a new force field for the layered silicates pyrophyllite, montmorillonite, and mica. Compared to experimental data, average deviations of unit cell parameters amount to ±0.5%, deviations of surface energies (or cleavage energies) to ±5%, and deviations of vibrational frequencies to less than 50 cm^{-1}. Distributions of charge defects in the minerals are modeled in agreement with solid-state NMR data. The reproduction of surface tensions, including their polar and dispersive contributions, corroborate the assignment of atomic charges on the basis of experimental X-ray deformation electron densities and a recent theoretical approach,[24] as well as our scheme to assign van der Waals parameters (section 2.6). Thus, the force field describes thermodynamics of surface processes more reliably by reducing common deviations of 50−500% in surface and interface energies to less than 10%, which is an important step toward quantitative modeling of interface processes involving layered silicates.

The force field parameters are suited for the PCFF (9-6 nonbond potential), CVFF (12-6 nonbond potential), and CHARMM and GROMACS (both 12-6 nonbond potential). Incorporation in biologically oriented force fields (CHARMM, GROMACS) allows the investigation of biologically oriented hybrid systems involving layered silicates. In contrast to some earlier models,[13,15,16,19] our semiempirical energy expression is also simpler (no exponential terms) and computationally less expensive.

As an example, we investigated the structure and dynamics of octadecylammonium chains on montmorillonite with a CEC of 90 mmol/100 g. The alkyl chains form a bilayer between the clay surfaces, and the ammonium headgroups are hydrogen-bonded to oxygen in the cavities on the clay

---

(64) He, H.; Frost, R. L.; Deng, F.; Zhu, J.; Wen, X.; Yuan, P. *Clays Clay Miner.* **2004**, *52*, 350−356.

surface. The mean squared displacement of the ammonium ions does not exceed (100 pm)^2 after long simulation times (2 ns), indicating the absence of rearrangements on the surface and a barrier for rearrangements greater than 5 kcal/mol. Chain conformations are significantly disordered, corresponding to a liquidlike state (4.6 gauche conformations per C_{18} chain at 25 °C and 5.4 gauche conformations per C_{18} chain at 100 °C). This might be associated with the low surface coverage with alkyl chains and is in agreement with the absence of a major phase transition on heating in DSC. Chain backbones cross over from one surface to the adjacent clay surface within the alkyl bilayer. Besides, very good agreement between experimental and simulated XRD patterns has been found, making the atomistic model helpful in understanding experimentally observed reflections.

Acknowledgment. We acknowledge support from the Air Force Office of Scientific Research. H.H. is grateful for a fellowship from the Air Force Research Laboratory. Discussions with Peter Mirau and Lawrence Drummy have been very valuable.

Supporting Information Available: Complete ref 11. This material is available free of charge via the Internet at http://pubs.acs.org.

CM0509328